Experimental and theoretical response of distributed read-out imaging devices with imperfect charge confinement

R. A. Hijmering,[1,a)] A. G. Kozorezov,[2] P. Verhoeve,[1] D. D. E. Martin,[1] J. K. Wigmore,[2] R. Venn,[3] and P. J. Groot[4]
[1]*Advanced Studies and Technology Preparation Division, Directorate of Science of the European Space Agency, ESTEC, P.O. Box 299, 2200 AG Noordwijk, The Netherlands*
[2]*Department of Physics, Lancaster University, Lancaster UK LA1 4YB, United Kingdom*
[3]*Cambridge MicroFab Ltd., Broadway, Bourn, Cambridgshire CB3 7TA, United Kingdom*
[4]*Department of Astrophysics, Radboud University, Nijmegen, P.O. Box 9010, 6500 GL Nijmegen, The Netherlands*

(Received 28 August 2009; accepted 24 January 2010; published online 28 April 2010)

We present a model to describe the responsivity of distributed read-out imaging devices following photon absorption in the absorber or in the base or top film of the superconducting tunnel junctions at either end of the absorber. The model describes the processes most relevant for photon detection, taking into account diffusion of quasiparticles across the absorber and imperfect confinement in the superconducting tunnel junctions via exchange of quasiparticles between absorber and the junction. It incorporates diffusion mismatch between superconducting tunnel junction and absorber, possible asymmetry between the two junctions and asymmetry between base and top electrodes within each junction. We have conducted dedicated experiments in which different experimental conditions were varied in order to test the model. A good agreement was found between the experimental results and model predictions. © *2010 American Institute of Physics*. [doi:10.1063/1.3327412]

I. INTRODUCTION

Cryogenic detectors, detectors which operate at sub-Kelvin temperatures, are being developed as photon counting spectrophotometers due to their excellent spectroscopic capabilities in UV, optical, and x-ray energies.[1] An important issue with these cryogenic detectors is to create a sufficiently large sensitive area while maintaining imaging capabilities and keeping the number of read-out channels within practical limits. Methods which are currently under investigation are multiplexed read-out of sensors and distributed read-out schemes which provide positional information within a sensor. Microcalorimeters with transition edge sensors (TES),[2] which measure the change in temperature due to the absorption of a photon through a change in resistance in the sensor, are usually read-out with superconducting quantum interference devices,[2] which provide a relatively easy multiplexing scheme. Depending on the application, a few tens to a few hundred detectors may be read-out through a single read-out channel. Kinetic inductance detectors (KIDs),[3] which rely on the change in inductance caused by the excitation of quasiparticles (qps) by the absorbed photon, can be grouped together on a single signal line by using a different resonance frequency for the read-out resonance circuit for each sensor. Superconducting tunnel junctions[4] (STJs) measure a photon-induced change in quasiparticle density as a tunnel current across a thin insulating barrier. Being high impedance devices, they are usually read-out with J-FET based charge sensitive preamplifiers, multiplexed read-out is not straightforward and distributed read-out is the more preferred approach. Distributed read-out imaging devices (DROIDs) (Ref. 5) consist of superconducting absorber strip with an STJ at either end. A photon is absorbed in the absorber strip and the excited quasiparticles will diffuse towards the STJs where they tunnel across the barrier and produce a measurable current pulse. The sum of the signals will provide information on the energy of the absorbed photon and the ratio of the signals will provide information on the position of the absorption site. A similar geometry is used with TESs as sensors, named DROIDs (Ref. 6) or position sensitive TES (Ref. 7), or with microwave kinetic inductance detectors (MKIDs) (Ref. 8) as sensors. The first relies on heat conduction to produce the change in temperature in the TESs and the latter relies on the diffusion of quasiparticles to produce a change in inductance in the MKIDs.

In the distributed read-out devices diffusion plays a major role in the detection process. The carriers diffuse from the absorption site towards the sensors where they produce a measurable signal. If the trapping (confinement of the signal carriers in the sensors, applicable to quasiparticles) is perfect they will remain in the sensor adding to the signal. If trapping is imperfect they will be able to escape from the sensor and diffuse towards the opposite sensor producing a crosstalk signal. This will reduce the ratio of the two charges, the time the charge carriers contribute to the signal and expose the signal carriers more to the losses inside of the absorber. All these effects will influence the position and energy resolution of the detector negatively.

Several groups have proposed theoretical models describing the DROID response. Kraus *et al.*[5] derived a widely used relation between the spectral and spatial resolution for DROIDs with perfect quasiparticle trapping in the STJs. Jochum *et al.*[9] have generalized this model in order to include imperfect quasiparticle trapping in the STJs by using a characteristic trapping time. Both models focused on the diffusion process of the signal carriers but excluded description of processes involved with the signal detection in the sensors.

a)Electronic mail: rhijmeri@rssd.esa.int.

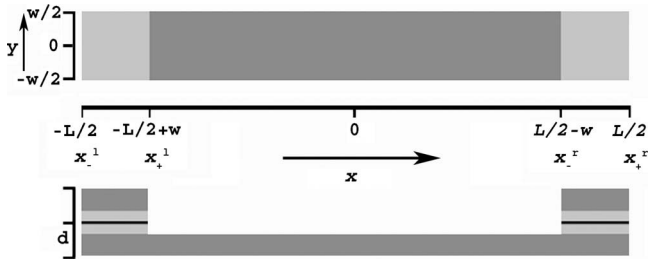

FIG. 1. Schematic representation of the DROID geometry with a top and side view, the thickness of the layers is greatly exaggerated.

Segall[10] and Savu *et al.*[11] developed a model for DROIDs which included the processes inside the STJs but assumes perfect trapping. Den Hartog *et al.*[12] produced a two-dimensional diffusion model of a DROID without trapping but accounting for quasiparticle dynamics in the STJ using Rothwarf–Taylor equations.[13] A similar model was developed by Ejrnaes *et al.*[14] using a different approach.

In this paper we describe a model for the responsivity of a DROID with STJs as sensors and imperfect trapping which describes all relevant dynamical processes for all photon absorption sites within the DROID. It has been tested against a responsivity data set from DROIDs with different geometries (Al thickness and absorber length) measured under varying operating conditions (bias voltage and temperature) using pulse sampling of the current pulses resulting from individual optical photons. The DROIDs used in this work consist of a pure tantalum absorber with a proximised Ta/Al STJ on either end.

II. MODELING OF DROID RESPONSE

We consider a DROID of length L (including the STJs) and width w consisting of a pure tantalum absorber with a Ta/Al STJ at either end, as shown in Fig. 1. The bottom tantalum layer of the STJs and the absorber are produced as a single layer on top of which the aluminum layer, barrier and top electrode of the STJs are grown. The presence of the aluminum in the STJs will decrease the energy gap of the STJs due to the proximity effect and provide confinement of quasiparticles. The STJs are square in geometry with the sides equal to the width of the absorber, and the thickness of a single Ta/Al bilayer is given by d. The coordinate along the length of the DROID is denoted by x and the position over the width of the DROID is denoted by y. The positions of the edges of the STJs in the x direction are at $x_-^l=-L/2$, $x_+^l=-L/2+w$, $x_-^r=L/2-w$, and $x_+^r=L/2$.

Differences in response between absorptions in the two STJs and/or between absorptions the top and base electrode of a single STJ may occur due to limitations in the fabrication process or initial experimental conditions. The parameters for either STJ are denoted by a superscript (i), left: $i=l$ and right: $i=r$. Similarly, subscript (j) is used to denote the top, $j=t$, and base, $j=b$, electrode. We also distinguish between the tunnel rate from the base electrode $(\Gamma_{t,bt}^{(i)})$ and from the top electrode $(\Gamma_{t,tb}^{(i)})$.

Within the complete system of the DROID we define different groups of quasiparticles divided by location and energy level. Figure 2 shows a schematic representation of the different groups of quasiparticles and, on the left hand side, the exchange routes between them. The first group are the quasiparticles inside the absorber $(Gr\ 1)$. These quasiparticles do not directly produce a signal, are subjected to the losses in the pure Ta absorber, are free to diffuse towards the STJs and are in the energy range $\varepsilon > \Delta_{\mathrm{Ta}}$. Second, quasiparticles inside the base electrode which have energies above the energy gap of the pure tantalum absorber form the second group $(Gr\ 2^{(i)})$. This group of quasiparticles will directly contribute to the signal by tunnelling across to the opposite electrode, they are subjected to the loss mechanisms inside the STJ base electrode, and since they are above the energy gap of the absorber they are free to diffuse out of the STJ into the absorber. The third group is formed by the quasiparticles which are in the base electrode of the STJ with energy below the energy gap of the absorber $(Gr\ 3^{(i)})$. Being confined within the STJ this group of quasiparticles differs from the previous group. Trapping efficiency of quasiparticles in the STJ affects the distribution of the quasiparticles between the second and third group. Quasiparticles from group 2 will feed group 3 via relaxation with emission of a phonon. This process, denoted by the relaxation rate $\gamma_s^{(i)}$, depends on the STJ proximisation and can be calculated.[15] Due to sequential tunnelling quasiparticles gain energy, equal to twice the applied bias voltage $(2\ \mathrm{eV}_b)$ with each tunnelling cycle, and after a sufficient number of cycles without relaxation the quasiparticles are promoted from group 3 into group 2. The number of tunnels needed to reach an energy above the energy gap of the absorber and thus to change the trapping efficiency can be adjusted for a given STJ lay-out with the bias voltage. In a biased STJ a quasistationary spectral distribution of quasiparticles is formed after one or two tunnelling events.[16] Therefore instead of modeling the complete dynamics in the STJ we ignore a short initial period and assume a quasistationary spectral distribution established in-

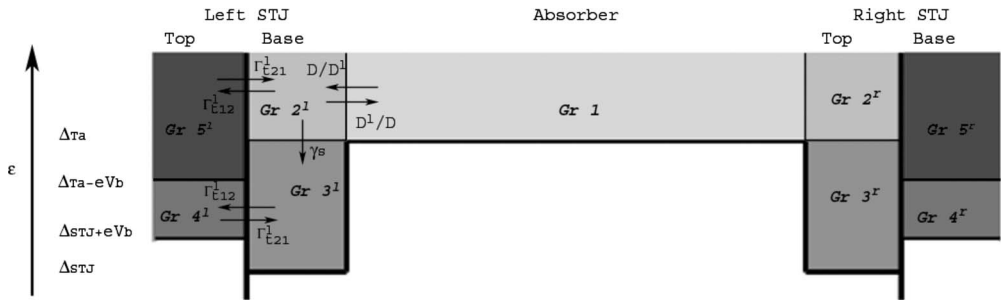

FIG. 2. Different groups of quasiparticles in a DROID which are determined by position in the DROID (horizontal scale) and energy (vertical scale).

stantly. Correspondingly for this distribution we divide the quasiparticles in the top film of the STJ into an energy group ($Gr\ 4^{(i)}$) which after tunnelling enters group 3 and an energy group ($Gr\ 5^{(i)}$) which after tunnelling enters group 2 and are free to diffuse into the absorber. The separation between these two groups is drawn at the energy $\Delta_{\mathrm{Ta}}-\mathrm{eV}_b$. We define $\xi^{(i)}$ to be the fraction of quasiparticles in the top electrode of the STJ with an energy above $\Delta_{\mathrm{Ta}}-\mathrm{eV}_b$. The quasiparticles in both these groups are subjected to losses in the top electrode.

Due to the suppressed gap in the proximised STJs of a DROID the responsivity of a photon absorption in the STJs is higher than that of a photon absorption in the absorber. This increase in responsivity is accounted for by the parameter χ. The efficiency of quasiparticle creation in proximized superconductors is lower compared to pure BCS-superconductors with the same energy gap.[17]

At the boundary between the absorber and STJ the spectrum of electronic excitations in a superconductor undergoes a transition from BCS-like (on the absorber side) to that of a proximised bilayer. As a result the transport parameters of quasiparticles will change on the scale of the coherence length. Particularly, a quasiparticle at an energy above Δ_{Ta} when it crosses the boundary will have a different diffusion coefficient, even though its elastic scattering rates may remain unchanged. This occurs because with the change in electronic spectrum the group velocity of the quasiparticles changes, leading to a change in diffusion coefficient. With the quasiparticle flux across the boundary being continuous this diffusion mismatch will affect the effective trapping of the quasiparticles inside the STJs. When the diffusion constant in the STJ is larger than in the absorber the quasiparticle density at the STJ side of the boundary will be depleted. In order to keep the quasiparticle flux continuous there will be a corresponding build up of their density on the absorber side leading to an increased injection into the STJ. Effectively, this will enhance trapping of quasiparticles in the STJs. For a lower diffusion constant in the STJ there will be a build up of quasiparticles at the STJ side of the boundary reducing the flux of quasiparticles into the STJ and thus reducing the effective trapping.

The presented DROID model also includes the situation when absorption takes place inside the STJ either in the top or base electrode. If the photon is absorbed in the base electrode the quasiparticles above the energy gap of the absorber can escape from the STJ before tunnelling. Thus only the fraction of quasiparticles created in the range $\Delta_g<\varepsilon<\Delta_{\mathrm{Ta}}$ are trapped within the STJ. The latter fraction is accounted for by the parameter $\beta^{(i)}$. If the absorption takes place in the top electrode of the STJ all quasiparticles must tunnel first before quasiparticles with sufficient energy can escape into the absorber increasing the responsivity. This additional contribution to the responsivity is accounted for by appropriate source terms in the Rothwarf–Taylor equations[13] describing photon absorption in the top or base electrode of the STJs. In the equation below the parameter α determines if there is an absorption in the top ($\alpha=0$) or base ($\alpha=1$) electrode. The Rothwarf–Taylor equation for the quasiparticle density in the base Ta film (group 1 and group 2) is given by

$$\frac{\partial n}{\partial t}-D\nabla^2 n+\gamma n+\sum_i\left[\Gamma^{(i)}_{t,bt}n-\xi^{(i)}\Gamma^{(i)}_{t,tb}n_t^{(i)}+(D-D_b^{(i)})\nabla^2 n-(\gamma-\gamma_s^{(i)}-\gamma_b^{(i)})n\right]\Theta(x_{i+}-x)\Theta(x-x_{i-})=\frac{N_0}{d}\delta(t)\delta(x-x_0)\left[\Theta\left(\frac{L}{2}-w-|x|\right)+\alpha[(1-\beta^{(i)})\Theta(x-x_-^{(i)})\Theta(x_+^{(i)}-x)]\right]. \quad (1)$$

For group 3 of the base film in the STJ we have

$$\frac{\partial n_b^{(i)}}{\partial t}-D_b^{(i)}\nabla^2 n_b^{(i)}+(\gamma_b^{(i)}+\Gamma^{(i)}_{t,bt})n_b^{(i)}-\Gamma^{(i)}_{t,tb}(1-\xi^{(i)})n_t^{(i)}-\gamma_s^{(i)}n=\frac{\alpha}{d}\beta^{(i)}N_{0g}^{(i)}\delta(t)\delta(x-x_0)\Theta(x_0-x_-^{(i)})\Theta(x_+^{(i)}-x_0). \quad (2)$$

Finally for the top film (group 4 and group 5)

$$\frac{\partial n_t^{(i)}}{\partial t}-D_t^{(i)}\nabla^2 n_t^{(i)}+(\gamma_t^{(i)}+\Gamma^{(i)}_{t,tb})n_t^{(i)}-\Gamma^{(i)}_{t,bt}(n_b^{(i)}-n)=\frac{(1-\alpha)}{d}[\beta^{(i)}N_{0g}^{(i)}+(1-\beta^{(i)})N_0]\delta(t)\delta(x-x_0)\Theta(x_0-x_-^{(i)})\Theta(x_+^{(i)}-x_0). \quad (3)$$

Here $\Theta(x)$ is the Heaviside step function, γ and $\gamma_{(j)}^{(i)}$ are the bulk loss rates in the absorber and in the base and top film of each STJ, γ_s is the inelastic relaxation rate of quasiparticles at $\varepsilon=\Delta_{\mathrm{Ta}}$, x_0 is the absorption position coordinate and N_0 and $N_{0g}^{(i)}$ are the number of created quasiparticles for an absorption in the absorber and STJ (i). Ideal edges at $\pm L/2$ are assumed meaning that the flux at the edges is zero resulting in the boundary condition:

$$D\left.\frac{du}{dx}\right|_{\pm L/2}=0.$$

The diffusion mismatch at the boundaries between the absorber and STJs results in the following boundary conditions:

$$D\left.\frac{du}{dx}\right|_{L/2-w-\delta}=D_b^l\left.\frac{du}{dx}\right|_{L/2-w+\delta},\quad D\left.\frac{du}{dx}\right|_{-L/2+w+\delta}=D_b^r\left.\frac{du}{dx}\right|_{-L/2+w-\delta},$$

$$u|_{L/2-w-\delta}=u|_{L/2-w+\delta},\quad u|_{-L/2+w+\delta}=u|_{-L/2+w-\delta}.$$

In order to solve Eqs. (1)–(3) it is convenient to find an appropriate set of orthogonal functions satisfying the boundary conditions which we introduced above. These functions u satisfy the equation

$$\frac{d}{dx}\left(D\frac{du}{dx}\right)+\kappa^2 Du=0.$$

For the set of orthogonal functions u we obtain the following expression:

$$u_m(x) = \sqrt{\frac{2}{L}} \begin{cases} \cos\kappa_m\left(\frac{L}{2}+x\right) + \left(1-\frac{D_b^l}{D}\right)\sin\kappa_m w \sin\kappa_m\left(\frac{L}{2}-w+x\right), & |x| \le \frac{L}{2}-w \\ \cos\kappa_m\left(x+\frac{L}{2}\right), & -\frac{L}{2} \le x \le -\frac{L}{2}+w \\ \left[\cos\kappa_m(L-w) + \left(1-\frac{D_b^r}{D}\right)\sin\kappa_m w \sin\kappa_m(L-2w)\right]\frac{\cos\kappa_m\left(x-\frac{L}{2}\right)}{\cos\kappa_m w}, & \frac{L}{2}-w \le x \le \frac{L}{2} \end{cases}. \tag{4}$$

Here κ_m is the m^{th} solution of the dispersion relationship:

$$\sin\kappa_m L + \frac{1-\frac{D_b^l D_b^r}{D^2}}{1+\frac{D_b^l D_b^r}{D^2}}\sin\kappa_m(L-2w) - \frac{\left(1-\frac{D_b^l}{D}\right)\left(1-\frac{D_b^r}{D}\right)}{1+\frac{D_b^l D_b^r}{D^2}}\cos\kappa_m(L-2w)\sin 2\kappa_m w = 0. \tag{5}$$

To solve the equations for the DROID model Eqs. (1)–(3) we look for the solutions in the form of an expansion over the functions $u_m(x)$ for x-direction and $u_n(y)$ for y-direction:

$$n(\bar{x},t) = \sum_{m,n} f_{m,n}\sqrt{\frac{D(x)}{\bar{D}}}u_m(x)u_n(y). \tag{6}$$

Here $D(x)$ is the profile of diffusion constants across the DROID

$$D(x) = D\Theta(L/2-w-|x|) + D_b^l\Theta(x_+^l-x)\Theta(x-x_-^l) + D_b^r\Theta(x_+^r-x)\Theta(x-x_-^r). \tag{7}$$

$\bar{D}$ is the mean diffusion constant given by

$$\bar{D} = D\{(L-2w)/L + w/L[(D_b^l+D_b^r)/D-2]\}, \tag{8}$$

and

$$u_n(y) = \sqrt{\frac{2}{w}}\cos n\pi\left(\frac{1}{2}+\frac{x}{w}\right). \tag{9}$$

For the STJs we may write:

$$n_{t/b}^{(i)}(\bar{x},t) = \sum_{m,n} f_{b/t.m,n}^{(i)}(t)v_m\left(x-x_-^{(i)}-\frac{w}{2}\right)u_n(y)\Theta(x - x_-^{(i)})\Theta(x_+^{(i)}-x) \tag{10}$$

where $v_m=(x-x_-^{(i)}-w/2)$ is another set of orthogonal functions for the range $x_-^{(i)}<x<x_+^{(i)}$ providing zero flux at all the edges of the STJ for quasiparticles in the base and the quasiparticles in the top electrode. For v_m we have:

$$v_m = \sqrt{\frac{2}{w}}\cos m\pi\left(\frac{1}{2}+\frac{x-x_-^{(i)}-w/2}{w}\right). \tag{11}$$

Inserting these expressions into Eq. (1) we obtain for the coefficients f_{m0} of Eq. (10) the following set of linear algebraic equations, in matrix notation:

$$\sum_{m'=1}^{\infty}\{\delta_{m',m}A_{m-1,0} - b(m-1,m'-1)\}F_{m'0} = g(m-1), \tag{12}$$

where F_{mn} is the matrix representation of f_{mn}. A_{mn} and $b(m,m')$ are given by:

$$A_{mn} = D\pi^2\left(\frac{m^2}{L^2}+\frac{n^2}{w^2}\right)+\gamma, \tag{13}$$

$$b(m,m') = \frac{1}{V(m)}\sum_i\left[(\Gamma_{t,bt}^{(i)} - A_{s,m'0}^{(i)})\frac{D(x)}{\bar{D}}J^{(i)}(m,m') - \xi^{(i)}\Gamma_{t,21}^{(i)}\sum_{m''}\frac{A_{b,m''0}^{(i)}\Gamma_{t,bt}^{(i)} + \gamma_s^{(i)}\Gamma_{t,bt}^{(i)}}{[A_{b,m''0}^{(i)}A_{t,m''0}^{(i)} - \Gamma_{t,bt}^{(i)}\Gamma_{t,tb}^{(i)}(1-\xi^{(i)})](1+\delta_{m''0})}\frac{D(x)}{\bar{D}}Y^{(i)} \times(m,m'')Y^{(i)}(m',m'')\right], \tag{14}$$

and $g(m)$ is given by:

$$g(m)=\frac{N_0}{V(m)}\frac{1}{4\pi d}\sqrt{\frac{2}{w}}\left\{\frac{D(x_0)}{\bar{D}}u_m(x_0)\left[\Theta\left(\frac{L}{2}-w-|x_0|\right)+\alpha\sum_i(1-\beta^{(i)})\Theta(x_+^{(i)}-x_0)\Theta(x_0-x_-^{(i)})\right]\right.$$
$$\left.+\sum_{(i)m'}\xi^{(i)}\Gamma_{t,tb}^{(i)}\frac{[(1-\alpha)(\beta^{(i)}\chi^{(i)}+1-\beta^{(i)})A_{b,m'0}^{(i)}+\alpha\beta^{(i)}\chi^{(i)}\Gamma_{t,bt}^{(i)}]}{A_{b,m'0}^{(i)}A_{t,m'0}^{(i)}-\Gamma_{t,bt}^{(i)}\Gamma_{t,tb}^{(i)}(1-\xi^{(i)})}\times\frac{v_{m'}^{(i)}(x_0)Y^{(i)}(m,m')}{1-\delta_{m'0}}\frac{D(x_0)}{\bar{D}}\Theta(x_+^{(i)}-x_0)\Theta(x_0-x_-^{(i)})\right\}. \quad (15)$$

Here:

$$J^{(i)}(m,m')=\int_{x_-^{(i)}}^{x_+^{(i)}}dx u_{m'}(x)u_m(x), \quad (16)$$

$$Y^{(i)}(m,m')=\int_{x_-^{(i)}}^{x_+^{(i)}}dx v_{m'}^{(i)}(x-x_-^{(i)}-w/2)u_m(x), \quad (17)$$

$$A_{b/t,mn}^{(i)}=D_{b/t}^{(i)}\frac{(n^2+m^2)\pi^2}{w^2}+\gamma_{b/t}^{(i)}+\Gamma_{t,bt/tb}^{(i)}, \quad (18)$$

$$A_{s,mn}^{(i)}=(D-D_b^{(i)})\kappa_m^2+\gamma-\gamma_s^{(i)}-\gamma_b^{(i)}, \quad (19)$$

and $V(m)$ is the normalization factor for the m^{th} harmonic $u_m(x)$

$$V(m)=2\delta_{m,0}\int_{-L/2}^{L/2}dx u_m^2(x).$$

In order to calculate the charge output of the two STJs we need to integrate the currents and find the total recorded charge. By definition the total recorded charge $Q^{(i)}(t)$ at an instant t by STJ (i) is given by

$$Q^{(i)}(t)=ed\int_0^t dt'\left[\Gamma_{t,bt}\int_{s^i}\int n(\bar{x},t')d\bar{x}+\Gamma_{t,tb}\times\int_{s^i}\int n^{(i)}(\bar{x},t')d\bar{x}\right] \quad (20)$$

Inserting Eqs. (6) and (10) and integrating over the time we get the following expression for the total charge $Q^{(i)}(t=\infty)$ of STJ (i) as a function of position:

$$Q^{(i)}=\pi ed\left[\sum_{m-0}^{\infty}f_{m0}(0)\sqrt{wL}\Gamma_{t,bt}\int_{x_-^{(i)}}^{x_+^{(i)}}dx\sqrt{\frac{D(x)}{\bar{D}}}u_m(x)+2w\Gamma_{t,tb}f_{b,00}^{(i)}(0)+2w\Gamma_{t,tb}f_{t,00}^{(i)}(0)\right]$$
$$=\pi ed\left(\sum_{m=0}^{\infty}f_{m,0}J\sqrt{wL}\left\{\Gamma_{t,bt}+\Gamma_{t,bt}\left[\frac{(\gamma_t+\Gamma_{t,tb})\gamma_s+\Gamma_{t,tb}\Gamma_{t,bt}(1-\xi)+\Gamma_{t,tb}(\gamma_b+\Gamma_{t,bt})+\gamma_s\Gamma_{t,tb}}{(\gamma_b+\Gamma_{t,bt})(\gamma_t+\Gamma_{t,tb})-\Gamma_{t,bt}\Gamma_{t,tb}(1-\xi)}\right]\right\}\right.$$
$$\left.+\frac{1}{2\pi d}\frac{\alpha\beta^{(i)}N_{0g}\Gamma_{t,bt}(\gamma_t+2\Gamma_{t,tb})+(1-\alpha)[\beta^{(i)}N_{0g}+(1-\beta^{(i)})N_0][(1-\xi)\Gamma_{t,bt}+(\gamma_b+\Gamma_{t,bt})]\Gamma_{t,tb}}{(\gamma_b+\Gamma_{t,bt})(\gamma_t+\Gamma_{t,tb})-\Gamma_{t,bt}\Gamma_{t,tb}(1-\xi)}\times\Theta(x_0-x_{i-})\Theta(x_{i+}-x_0)\right). \quad (21)$$

The values for $f_{m,0}$ are obtained by solving the set of linear algebraic equations of Eq. (12).

III. EXPERIMENTAL SET-UP AND DATA REDUCTION

DROIDs, produced by Cambridge MicroFab Ltd,[17,18] with different Ta/Al STJs have been used to test the described model. The STJs consist of a Ta/Al/AlO_x/Al/Ta multilayer with thicknesses of: 100/30/1/30/100, 100/60/1/60/100, and 100/100/1/100/100 nm and energy gaps (Δ_{STJ}), as measured from the current-voltage curves, of: 500, 420 and 360 μeV, respectively. The (residual resistance ratio) (*RRR*) values for the base Ta layer as measured using a dedicated structure on the chip are 37.2, 43.6, and 30.2 for the DROID with 30, 60, and 100 nm thick Al trapping layer, respectively. For all three lay-ups a DROID of 400 μm in length, including STJs, and a width of 30 μm is used as a reference device. The STJs are square in geometry with the sides equal to the width of the absorber. The 100 nm thick pure tantalum absorber and the tantalum layer of the base electrode of the STJs are part of the same epitaxial Ta layer (see Fig. 1). The resolving powers at 2.5 eV of the devices are: 10, 8, and 5 for the aluminum thicknesses of 30, 60, and 100 nm, respectively. It must be mentioned that the used experimental set-up was fully optimised to measure the true responsivity of the DROIDs, as indicated below, and not optimized to measure the energy resolution introducing extra electronic noise. As a result the given values for the resolving powers should be seen as lower limits and the true

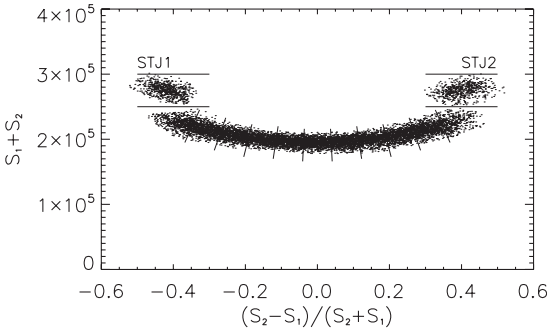

FIG. 3. Scatter plot of the sum vs normalized ratio of the result from the simulated shaping stages. Events from the STJs can be easily distinguished and selected by their spatial separation. The absorber events are divided into 11 sections along the position direction.

resolving power will lie slightly higher.

A ^{3}He sorption cooler with a base temperature of 280 mK, low enough to reduce the thermal current to a negligible level for all three device structures, has been used to conduct the measurements. The cryostat is equipped with an optical fiber to illuminate the chip through the sapphire substrate with optical photons ($E_0=1-5$ eV) from a Xe lamp filtered by a double grating monochromator. In this set-up it is only possible to illuminate the devices through the sapphire substrate and only the case where $\alpha=0$ (base electrode illumination) could be investigated.

The signal pulses from the STJs are fed into a charge sensitive preamplifier with a RC time of 470 μs at ambient temperature and subsequently digitized with a computer oscilloscope card (GaGe CS14100). With simulated shaping filters a measure of the responsivity can be obtained from the preamplifier signal to make a first selection of the events. Figure 3 shows a scatter plot of individual photon signals after the simulated shaping stages in an S_1+S_2 (a measure for the energy) versus $(S_1-S_2)/(S_1+S_2)$ (a measure for the position) representation. The STJ events can easily be distinguished by their spatial and spectral separation. Using the results from the simulated shaping stage the noise events are removed and the remaining events are divided into 13 sections based on the position (11 sections on the absorber and the two STJs). The preamplifier pulses of the events in a single section are averaged to obtain a low noise charge pulse. Averaging of the charge pulses is possible because the position resolving power ($L/\Delta x$) of the absorber is below 11. From the average charge pulses the preamp response is deconvoluted to reduce the integration time and electronic noise. The resulting photocurrent pulses, one per section, are integrated to obtain the true charge output.

These average values of the charge output are used to test the model. In order to obtain an objective fit of the model to the data set a least squared fitting routine is used.

The model presented in this paper is described in the most generalized version with separate parameters for the each of the groups described in Sec. II and the possibility to distinguish between top and base illumination. With the current data set it is not possible to distinguish between the top and base electrodes and the corresponding parameters for the two electrodes have therefore been replaced by a single common parameter. These parameters are the tunnel rates: $\Gamma_t^{(i)}=\Gamma_{t,bt}^{(i)}=\Gamma_{t,tb}^{(i)}$, the diffusion constants in the STJs: $D^{(i)}=D_b^{(i)}=D_t^{(i)}$ and the loss rates in the STJs: $\gamma^{(i)}=\gamma_b^{(i)}=\gamma_t^{(i)}$. The parameters shown in Table I could be calculated or estimated and are kept fixed within the model. These are; $\gamma_s^{(i)}$ the relaxation rate at $\varepsilon=\Delta_{Ta}$, $\beta^{(i)}$ the fraction of quasiparticles created in the range $\Delta_g<\varepsilon<\Delta_{Ta}$. The ratio between the responsivity of the STJ and absorber, $\chi^{(i)}$, are calculated using the models described in Refs. 15 and 17.

TABLE I. Values of the fixed parameters. The values are calculated separately using different models.

	Symbols	30 nm	60 nm	100 nm
Relaxation rate	γ_s^l, γ_s^r	1×10^6 s^{-1}	2×10^6 s^{-1}	3.5×10^6 s^{-1}
QPs in $\Delta_g<\varepsilon<\Delta_{Ta}$	β^l, β^r	0.75	0.78	0.8
Ratio of responsivities	χ^l, χ^r	1.17	1.3	1.5

The operating and device parameters have been varied for devices of several geometries in order to thoroughly test the parameters of the model for their correct description of the processes.

IV. COMPARISON BETWEEN THE THEORY AND THE EXPERIMENTAL RESULTS

All three reference devices were illuminated by photon with energies within the range 1–5 eV. The measurements have been conducted at an operating temperature of 295 mK and at a bias voltage of 100 μV in most of the tests on the DROID with 30 nm aluminum trapping layers and 150 μV for the DROIDs with 60 and 100 nm aluminum trapping layers. This difference in bias voltage only affects the value of $\xi^{(i)}$ and a measurement with the DROID with 30 nm aluminum trapping layers using a bias voltage of 150 μV has been added to the results for comparison.

The model predicts the charge output of each STJ as a function of absorption position in the absorber or in the STJ. However, from the measurements only the two charges are known. In order to fit the results from the model to the measured data both are converted into a Q_r versus $(Q_l-Q_r)/(Q_l+Q_r)$ graph, and fitted using a least-squares fit. Figure 4 shows an example of fits of the model to measurements for the three reference devices at photon energy of 5 eV. To confirm the correctness of the fit the measured data is plotted as Q_l versus $(Q_l-Q_r)/(Q_l+Q_r)$ with the result of the model, in the same representation, over plotted.

In all the cases the model satisfactorily describes the data points of the absorber events as well as the STJ events. The data from the DROID with 100 nm aluminum [Fig. 4(d)] trapping layer shows a significant asymmetry between the STJs, caused by an accidental difference in bias voltage, which is correctly described by the model as a variation in the value for ξ^r. This case also shows some discrepancy between the fit and the measurement due to the increased uncertainty on the measurement.

The results of the fit of the model to the data for different photon energies are constant within the accuracy of the measurement and the measured charge output is proportional to the input photon energies. Table II shows the average values

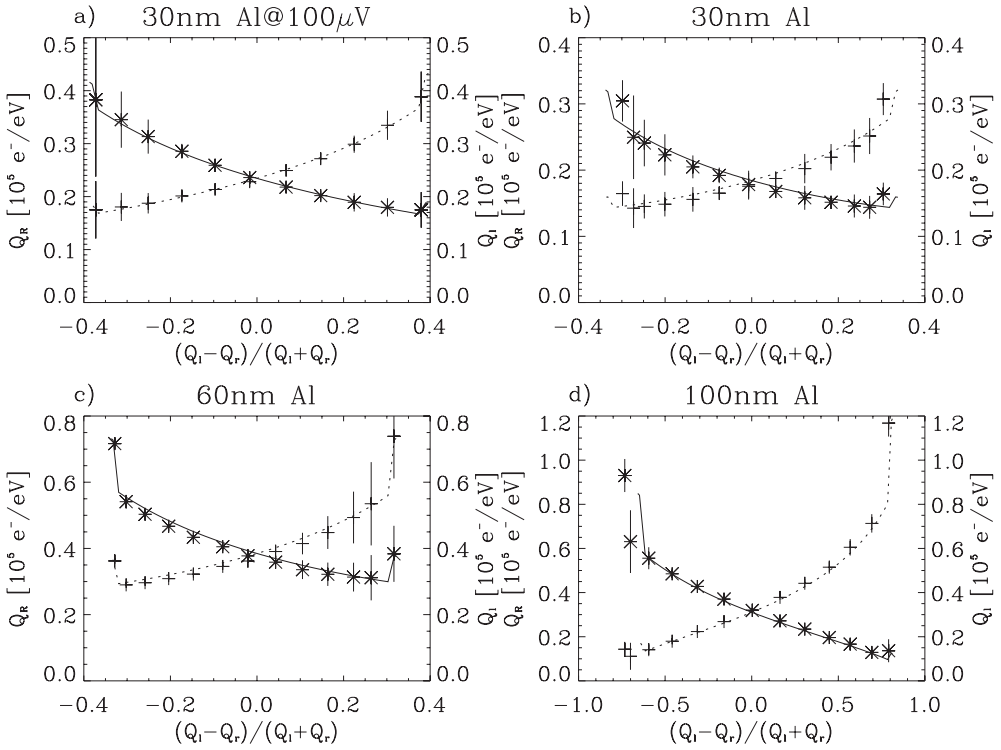

FIG. 4. The fit of the model to the measured charge output of the three DROID geometries. Each graph shows the charge output of the two STJs vs normalized charge ratio, (asterisk for Q_r, plus sign for Q_l), with the fit of the model over plotted, solid lines. The dashed line is the calculated Q_l from the fit results. All measurements are from an illumination with 5 eV photons at an operating temperature of 295 mK. (a) Shows the responsivity of the DROID with 30 nm aluminum trapping layers at 100 μV. (b) Shows a measurement from the same device with the same settings but biased at a voltage of 150 μV for direct comparison with the other devices, and [(c) and (d)] show measurements for the DROIDs with 60 and 100 nm aluminum trapping layers, respectively.

for the parameters obtained from the fits of the model to the data sets obtained at different photon energies with the uncertainties being the standard deviations. The values of $\xi^{(i)}$ for the 30 nm aluminum trapping layer DROID corresponding with a measurement at 150 μV have been added in parenthesis.

Single STJs produced on the same wafer as the DROIDs enable an independent and more direct measurement of the tunnel rate. The values for the tunnel rate obtained from the fit to the DROID data agree with the values obtained from single STJs of the same wafer agree within the uncertainties. These values lay within the expected range based on our previous experience with this STJ lay-out.

Thicker aluminum on top of the tantalum layer in the STJ reduces the energy gap in the STJ with respect to the bulk tantalum gap in the absorber. Therefore, more quasiparticles will reside below Δ_{Ta} and the trapping efficiency is increased such that fewer quasiparticles generated in one STJ can escape to the other STJ. In Fig. 4 the effect of improved trapping with larger aluminum thickness can be seen as a larger separation of the two STJs along the $(Q_l-Q_r)/(Q_l+Q_r)$ axis. Within the model this effect is described by the value for the fraction of quasiparticles above $\Delta_{Ta}-eV_b$, $\xi^{(i)}$, which decreases with increasing aluminum thickness, at a constant bias voltage.

TABLE II. The average parameters resulting from the fit of the model to the experimental data obtained with the reference device at $T=295$ mK and $V_b=150$ μV, for 60 and 100 nm Al layer, and $V_b=100$ μV, for 30 nm Al layer.

	Symbols	30 nm	60 nm	100 nm
Tunnel rates	$\Gamma_t^l(10^5\ s^{-1})$	23 ± 1	26 ± 3	34 ± 3
	$\Gamma_t^r(10^5\ s^{-1})$	22 ± 1	27 ± 4	33 ± 3
QP above ΔTa	ξ^l	0.49 (0.6)[a] ±0.02	0.36 ± 0.03	0.12 ± 0.01
	ξ^r	0.49 (0.6)[a] ±0.02	0.35 ± 0.03	0.16 ± 0.01
Diffusion constant	$D(10^4\ cm^2/s)$	24.7 ± 0.8	23.1 ± 0.3	23.3 ± 0.3
	$D^l(10^4\ cm^2/s)$	24.3 ± 0.1	23.1 ± 0.7	24.2 ± 0.2
	$D^r(10^4\ cm^2/s)$	24.6 ± 0.1	23.1 ± 0.3	22.6 ± 0.5
Loss rates	$\gamma\ s^{-1}$	$17\,900\pm600$	$14\,200\pm200$	$33\,000\pm2000$
	$\gamma^l\ s^{-1}$	5700 ± 2000	5500 ± 500	$11\,000\pm1000$
	$\gamma^r\ s^{-1}$	6100 ± 2000	4500 ± 400	$11\,500\pm1600$

[a]For the 30 nm aluminum trapping layer device the value for $\xi^{(i)}$ at a bias voltage of 150 μV has been added for comparison with the results from the other DROIDs.

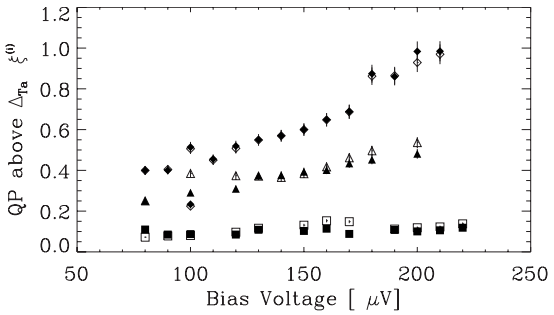

FIG. 5. Fitted values for the fraction of quasiparticles above Δ_{Ta} ($\xi^{(i)}$) as a function of bias voltage for the DROIDs with 30 nm (diamonds), 60 nm (triangles), and 100 nm (squares) aluminum trapping layers. The filled symbols are for the left STJ and the open symbols are for the right STJ.

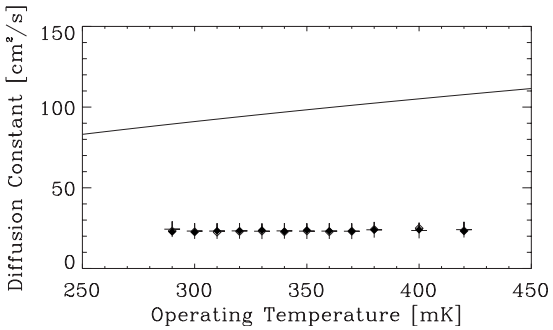

FIG. 6. Diffusion constant vs temperature for the DROID with 30 nm aluminum trapping layers. The different symbols denote the diffusion constant in the absorber (crosses), left STJ (open diamonds), and right STJ (filled diamonds). The solid line denotes the theoretical diffusion constant as predicted by Eq. (22).

Further confirmation of the correct description of the parameter $\xi^{(i)}$ is obtained from a scan in bias voltage for all three DROID geometries. These measurements have been conducted at an operating temperature of 295 mK. The DROID with 30 nm aluminum trapping layers was illuminated with 5 eV photons while the 60 and 100 nm were illuminated with 4.1 eV photons. All parameters of the model are the same as in Table II within the uncertainties of the measurement, except for $\xi^{(i)}$ which increases with bias voltage (Fig. 5) as expected. The value for $\xi^{(i)}$ for the DROID with 30 nm aluminum layer increases from 0.4 at 90 μV and reaches unity at 200 μV, corresponding to a complete absence of confinement. This voltage is equal to the difference of the energy gaps of the STJ and absorber and all quasiparticles indeed remain above $\Delta_{Ta}-eV_b$.

For a photon absorption in one of the STJs of a DROID with perfect trapping ($\xi^{(i)}=0$) the charge output of the opposite STJ is equal to zero and in the representation of Fig. 4 these events will occur on a single vertical line with $(Q_l-Q_r)/(Q_l+Q_r)$ equal to 1 or -1. Any noise in the opposite STJ may give false triggers, of which only those with positive Q are registered. This can give rise to a small artificial shift in the STJ signal in the scatter plots away from the vertical line at ± 1. For this reason it is expected that the trapping in the DROID with 100 nm aluminum trapping layers is slightly underestimated (and hence the value of $\xi^{(i)}$ is overestimated), in particular, at lower bias values.

The lack of variation in diffusion constant, as shown by the results in Table II, between the three DROIDs indicates no connection between the *RRR* value, which is varying from device to device, and the nonequilibrium quasiparticle diffusion properties of the material. When quasiparticles thermalise while being in the absorber the following expression for the diffusion constant in the absorber would apply:

$$D \cong \frac{1}{3}\sqrt{\frac{2kT_{qp}}{\pi\Delta_{Ta}}}\upsilon_F\lambda_{300}RRR, \tag{22}$$

with T_{qp} the temperature of the quasiparticles in the absorber (taken equal to the operating temperature), ν_F the Fermi velocity (0.67×10^6 m/s as taken from literature[19]) and λ_{300} the mean free path at room temperature (7 nm calculated using the Drude model[20] from the measured resistance).

The DROID with 30 nm aluminum trapping layers was illuminated using 5 eV photons at bias voltage of 100 μV at different operating temperatures, limited by the base temperature of the cryostat at the low end and thermal noise contribution at the high end. Figure 6 shows the different diffusion constants of the Ta absorber resulting from the fit of the model to the data; all other parameters of the model remain the same within the uncertainties of the measurement as the values from Table II. The solid line shows the theoretical prediction of Eq. (22) which is well above of the experimental values. However, the measured values are in agreement with previously obtained values on Ta/Al DROIDs from a different manufacturer[21] and with values obtained by other groups.[22–24]

As seen in Table II there is no noticeable diffusion mismatch between the absorber and the STJs in any of the three DROID geometries. As described the tantalum absorber is only in contact to the tantalum layer of the base electrode and in order to estimate the diffusion mismatch between the absorber and the STJ only the quasiparticle energy distribution in the tantalum layer of the STJ above an energy equal to Δ_{Ta} has to be compared to the energy distribution in the BCS-like tantalum absorber. Figure 7 shows the density of states (DOS) for the BCS-like absorber and for a proximised Ta/Al bilayer with thicknesses 100/30 nm. Both show a maximum at Δ_{Ta} and rapid decay of the DOS towards high energy levels. In both situations the majority of the quasiparticles will remain near Δ_{Ta} with rapid depletion at higher energies producing little difference in the quasiparticle dis-

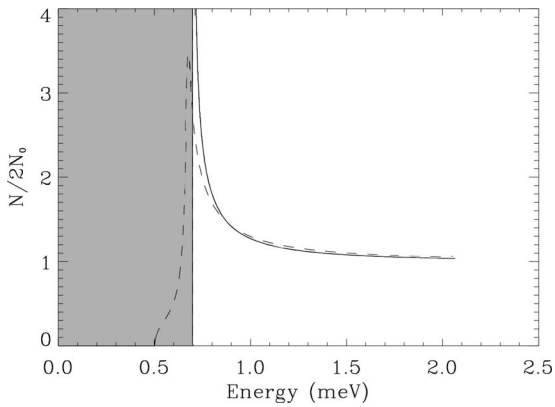

FIG. 7. DOS of the BCS tantalum absorber (solid line) and Ta/Al STJ (dashed line).

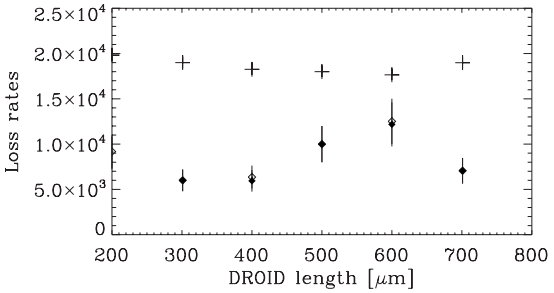

FIG. 8. Loss rates in the DROIDs with different lengths from 30 nm Al series. The loss rate in the absorber (crosses) is constant indicating homogeneous tantalum layer quality. The loss rate in the STJs (diamonds, open: left and filled: right) shows scatter between the DROIDs. This is caused by differences in plug quality.

tribution. We expect that the diffusion mismatch for this device will be below the accuracy of the data set.

Previous results[15] on STJs have indicated that quasiparticle losses inside the STJ are due to bulk material losses and a concentration of loss centers near the leads, especially the plugs which are made of higher gap material to avoid outdiffusion of quasiparticles. Recent developments have indicated that quasiparticle losses in superconducting materials may be due to a very small amount of magnetic impurities in the high grade superconducting material.[25–27] The number of these impurities as well as the quality of the plugs, and thus the value of the loss rate are difficult to control in the production process, as indicated by the scatter in loss rate between the three devices. The DROID with 100 nm Al trapping layer shows an increased loss rate in the absorber. This device has been produced in another but similar deposition system with a different sputter target. Compared with the STJ the loss rates in the absorber are much higher for all three devices indicating that the loss centers are mainly concentrated in the tantalum. The quasiparticles in the tantalum absorber are fully exposed to these loss centers while in the STJ the quasiparticles partly remain in the aluminum away from these loss centers. This is in agreement with our experience with pure aluminum devices which show extremely low loss rates.

Figure 8 shows the result of DROIDs of different lengths, ranging from 200 to 700 μm, with 30 nm aluminum layers in the STJs. The DROIDs were grown on a single chip and they have been measured within a single measurement run assuring similar fabrication and measurement conditions. The results can be described by the model using the parameters from Table II and changing the length of the DROID. The loss rate of the absorber remains constant for the different DROIDs indicating a homogeneous tantalum layer quality over the chip. However, the loss rate within the STJ varies from DROID to DROID indicating that the quality of the niobium plugs varies over the chip. This scatter in plug quality can also explain the absence of a correlation between the thickness of the aluminum layer and the difference of loss rate in the STJ and absorber.

Using the loss rate of the absorbers and the determined diffusion constant we can determine the value of the loss length $\Lambda = \sqrt{D\tau_{\mathrm{loss}}}$. The obtained values are: 370, 403, and 266 μm for the DROIDs with Al thickness of 30, 60, and 100 nm. This is slightly larger then earlier reported values by our group,[21] 285 μm, which was with a different manufacturer. It is also larger then values reported by another group,[10] 160 μm, which can indicate a higher quality of epitaxial Ta film.

V. DISCUSSION

We have presented a theoretical model that describes the most important processes involved with photon detection using DROIDs. When the proper assumptions are made all previously obtained models follow as limiting cases, which has been tested. For example when no proximization of the base electrode is assumed the results from den Hartog[12] and from Ejrnaes[14] follow. Similarly, the results from Kraus[5] follow in the limit of immediate and full thermalization of the quasiparticles once they enter the STJ area. And the results from Jochum[9] also follow from this model when the diffusion mismatch is ignored and the quasiparticles confined in the STJs are not able to gain energy to leave the STJ and go into the absorber.

We have tested the model against a set of experimental data of integrated signal charge from DROIDs using a least-squares fitting method and found good agreement with the experimental results. Using this model and a single set of parameters for each DROID we were able to describe the data set with all the DROID parameters within the expected range. The model correctly describes the DROID responsivity for absorption in both the absorber and the STJs with use of the separately calculated parameters $\chi^{(i)}$ and $\beta^{(i)}$. The tunnel rates obtained for the different STJ geometries are in agreement with values obtained for single devices on the same wafer. Even asymmetry between the two STJs can easily be handled by the model as shown by the fit in Fig. 4(d).

The variation in the parameter $\xi^{(i)}$ shows increased trapping efficiency with increasing aluminum thickness, as expected due to the decrease in energy gap of the STJ (Table II), and also with decreasing bias voltage (Fig. 5), as expected from its definition, as the fraction of number of quasiparticles above $\Delta_{\mathrm{Ta}} - \mathrm{eV}_b$. The scan in bias voltage for the DROID with 30 nm aluminum trapping layer further provides proof of the correctness of these parameters. In this scan the parameter $\xi^{(i)}$ reaches unity at the bias voltage at which $\Delta_{\mathrm{Ta}} - \mathrm{eV}_b$ is equal to the energy gap of the STJ.

The diffusion constants for the three DROIDs are found to be the same and show no dependence on operating temperature or *RRR* value. Although no correct theoretical description is available for the value of the diffusion constant the obtained value does agree with several other independent measurements of the diffusion constant in tantalum absorbers of DROIDs.

Unfortunately the quasiparticle distribution (Fig. 7) shows little change at the interface between the absorber and STJ no significant diffusion mismatch is present in this DROID geometry, which makes it impossible to test the role of this process.

Using a single parameter set, with exception of the loss rate in the STJ, the model was able to describe the results of several DROIDs of different lengths, located on a single chip

and measured within a single run, showing the rigidity of the model. Within the fabrication process losses in the devices are still an important unknown factor, which makes the result uncertain from device to device. However, the behavior of the loss rate within the different materials (low losses in the aluminum, higher losses in the tantalum and scatter in plug quality over the chip) agrees with our previous experiences.

VI. CONCLUSION

We have developed a model to describe the integrated signal charge resulting from the detection of photons using DROIDs. The model incorporates all the important processes in the absorber and STJ involved with the photon detection. Tests of the model against responsivity data obtained from illumination with optical photons have shown the possibility of describing this data set using a uniform parameter set. Tests of the individual model parameters have shown they respond as expected to changes in the experimental conditions. The model can be used to characterize and predict the behavior of DROID used as photon detectors.

[1]N. Sullivan, H. Meyer, and M. Paalanen, J. Low Temp. Phys. **151** (2008).
[2]K. D. Irwin, Appl. Phys. Lett. **66**, 1998 (1995).
[3]P. Day, H. Leduc, B. Mazin, A. Vayonakis, and J. Zmuidzinas, Nature (London) **425**, 817 (2003).
[4]A. Peacock, P. Verhoeve, N. Rando, A. van Dordrecht, B. G. Taylor, C. Erd, M. A. C. Perryman, R. Venn, J. Howlett, D. J. Goldie, J. Lumley, and M. Wallis, Nature **381**, 135 (1996).
[5]H. Kraus, F. v. Feilitzsch, J. Jochum, R. L. Mössbauer, Th. Peterreins, and F. Pröbst, Phys. Lett. B **231**, 195 (1989).
[6]S. J. Smith, C. Whitford, G. W. Fraser, A. D. Holland, D. Goldie, T. J. R. Ashton, R. J. Limpenny, and T. Stevenson, Nucl. Instrum. Methods Phys. Res. A **520**, 449 (2004).
[7]E. Figueroa-Feliciano, J. Chervenak, F. M. Finkbeiner, M. Li, M. A. lindeman, C. K. Stahle, and C. M. Stahle, AIP Conf. Proc., **605**(1), 239 (2002).
[8]B. A. Mazin, M. E. Eckhart, B. Bumble, S. Golwala, P. K. Day, I. Gao, and J. Zmuidzinas, J. Low Temp. Phys. **151**, 537 (2008).
[9]J. Jochum, H. Kraus, M. Gutsche, B. Kemmather, F. v. Feillitzsch, and R. L. Mössbauer, Ann. Phys. (N.Y.) **2**, 611 (1993).
[10]K. Segall, Ph.D. thesis, Yale University, 2000.
[11]V. Savu, L. Li, A. Mukherjee, C. M. Wilson, L. Frunzio, D. E. Prober, and R. J. Schoelkopf, Nucl. Instrum. Methods **520**, 237 (2004).
[12]R. H. den Hartog, D. Martin, A. G. Kozorezov, P. Verhoeve, N. Rando, A. Peacock, G. Brammertz, M. Kramrey, D. Goldie, and R. Venn, Proc. SPIE **4012**, 237 (2000).
[13]A. Rothwarf and B. N. Taylor, Phys. Rev. Lett. **19**, 27 (1967).
[14]M. Ejrnaes, C. Nappi, and R. Cristiano, Supercond. Sci. Technol. **18**, 953 (2005).
[15]A. G. Kozorezov, R. A. Hijmering, G. Brammertz, J. K. Wigmore, A. Peacock, D. Martin, P. Verhoeve, A. A. Golubov, and H. Rogalla, Phys. Rev. B **77**, 014501 (2008).
[16]G. Brammertz, Ph.D. thesis, Universiteit Twente, 2003.
[17]R. A. Hijmering, P. Verhoeve, D. D. E. Martin, A. G. Kozorezov, J. K. Wigmore, R. Venn, P. J. Groot, and I. Jerjen, J. Appl. Phys. **105**, 123906 (2009).
[18]D. D. E. Martin, Ph.D. thesis, University Twente, 2007.
[19]B. Chakraborty, W. E. Pickett, and P. B. Allen, Phys. Rev. B **14**, 3227 (1976).
[20]P. Drude, Ann. Phys. **306**, 566 (1900).
[21]R. den Hartog, A. Kozorezov, D. Martin, G. Brammertz, P. Verhoeve, A. Peacock, F. Scholze, and D. J. Goldie, AIP Conf. Proc., **605**, 11 (2002).
[22]M. L. van den Berg, Ph.D. thesis, Utrecht University, 1999.
[23]P. Verhoeve, S. Kraft, N. Rando, A. Peacock, A. van Dordrecht, R. den Hartog, D. J.Goldie, R. Hart, and D. Glowacka, IEEE Trans. Appl. Supercond. **9**(2), 3342 (1999).
[24]S. Friedrich, M. C. Gaidis, C. M. Wilson, D. E. Prober, A. E. Szymkowiak, and S. H. Moseley, Appl. Phys. Lett. **71**, 3901 (1997).
[25]R. A. Hijmering, A. G. Kozorezov, A. A. Golubov, P. Verhoeve, D. D. E. Martin, J. K. Wigmore, and I. Jerjen, IEEE Trans. Appl. Supercond. **19**(3), 423 (2009).
[26]A. G. Kozorezov, A. A. Golubov, J. K. Wigmore, D. Martin, P. Verhoeve, R. A. Hijmering, and I. Jerjen, Phys. Rev. B **78**, 174501 (2008).
[27]R. Barends, J. J. Baselmans, S. J. C. Yates, J. R. Gao, J. N. Hovenier, and T. M. Klapwijk, Phys. Rev. Lett. **100**, 257002 (2008).